Applied Surface Science 565 (2021) 150462

Contents lists available at ScienceDirect

Applied Surface Science

journal homepage: www.elsevier.com/locate/apsusc

Full Length Article

Weak enthalpy-interaction-element-modulated NbMoTaW high-entropy alloy thin films

Linxia Bi [a], Xiaona Li [a,*], Yinglin Hu [a], Junyi Zhang [a], Xiao Wang [a], Xuecheng Cai [b], Tongde Shen [b], Renwei Liu [c], Qing Wang [a,d], Chuang Dong [a], Peter K. Liaw [a,d]

[a] Key Laboratory of Materials Modification by Laser, Ion and Electron Beams (Ministry of Education), School of Materials Science and Engineering, Dalian University of Technology, Dalian 116024, China
[b] Clean Nano Energy Center, State Key Laboratory of Metastable Materials Science and Technology, Yanshan University, Qinhuangdao 066004, PR China
[c] Shimadzu China Co. LTD, Shanghai 200233, China
[d] Department of Materials Science and Engineering, The University of Tennessee, Knoxville, TN 37996, USA

ARTICLE INFO

Keywords:
Refractory high-entropy film
Local structure
Cluster-plus-glue-atom
Thermal stability

ABSTRACT

A local structure determines the properties in disordered solid solutions with simple crystal structure. Introducing a weak enthalpy-interaction-element will change the local structure evolution of refractory high-entropy alloy films, thereby bringing effects for the properties. Herein series of $(NbMoTaW)_{100-x}V_x$ ($x = 0 \sim 30.5$, at%) thin films were prepared by radio frequency magnetron sputtering, and systematic investigations of the films are carried out through combining the underlying microstructure, mechanical properties, and resistivity-temperature behavior. Furtherly, in accordance with the cluster-plus-glue-atom model, the present paper interpreted the local structure evolution with the film components changing. The results reveal that the excellent thermal stability of the films is originate from the enthalpy interaction, and the high stability of the refractory element itself. The V addition is free of crystal structure variation in the films, but bringing two-fold effects. The main one is the enhancement of the microstructural homogeneity by increasing the disorder degree. The other is weakening interatomic interactions as well as enabling the films more unstable due to the increasing system energy. The refractory high-entropy films can be promising candidates for high temperature, high hardness, and wear-resistance applications, e.g., high-temperature-bearing structures, heat-protection systems, diffusion barriers, and film resistors.

1. Introduction

Multicomponent alloys in near-equal molar ratios are considered to be disordered solid solutions with simple crystal structures [1,2]. Theoretically, high temperature excepted, it is hard to obtain ideally-mixed solid solutions due to existence of enthalpic interactions [3]. Meanwhile, the difference in mixing enthalpies between elements can induce the diversity of a local chemical order (LCO) in multi-principal-component alloys, heightening the ruggedness of the energy landscape and increasing the difficulty of activation of dislocation movement. Thus, the selection of dislocation pathways in slip, faulting, and twinning are affected, and the lattice friction to dislocation motion through a nanoscale-segment detrapping mechanism is increased. Furthermore, experimental studies also have shown [4] that an alloying element, Pd, with distinct difference in the atomic size and electronegativity was introduced into the CrMnFeCoNi system, producing a significant component fluctuation at the nanoscale, which further resulting in alternate tensile and compressive strain fields. It not only promotes the increase of the stacking fault energy through inhibiting the dislocation slip, but also generates a large amount of dislocation cross slip, which can achieve higher yield strength without affecting strain hardening and tensile ductility. Therefore, the local structure is a crucial factor for properties of disordered solid-solution alloys with single structures.

Adding a disturbing component is regarded as an effective strategy for altering the local structure. According to the distinction between disturbing and principal components, it results in either forming a more homogeneous disorder solid solution or more difference in local structures (exhibiting greater micro-segregation), which is also beneficial to performance modulation. In the AlCoCrFeNi alloy, after adding V, the segregation of Al, Ni, and Fe is significantly reduced, and the

* Corresponding author.
E-mail address: lixiaona@dlut.edu.cn (X. Li).

https://doi.org/10.1016/j.apsusc.2021.150462
Received 10 May 2021; Received in revised form 22 June 2021; Accepted 22 June 2021
Available online 28 June 2021

microstructure is more uniform. Meanwhile, with the increase of the V content, the yield strength and hardness improve from 1,378.9 MPa to 1,726.5 MPa and HV534 to HV648.8, respectively [5]. Introducing Nb into the CoCrCuFeNi high-entropy coating can induce the precipitation of the Nb-rich phase and Cu segregation, increasing its wear resistance by 1.5 times [6]. The Re addition in the NbMoTaW bulk alloy would form (Nb, Ta)-enriched granular phases except for the body-centered-cubic (BCC) phase, which greatly improves the room-temperature (RT) yield strength and plasticity of the alloy [7]. Similar results also can be obtained even in the medium entropy alloy, e.g., when a slight mount of refractory element, W, added into the CrCoNi alloy, reducing the elemental distribution homogeneity significantly and improving the mechanical properties [4]. The present work concentrates on the correlation between the local structure and strength. However, rare regularity investigations are performed for the influence of disturbing component on the local structure and properties. Additionally, alloy stability is closely related to the applications, but what is the relationship between the stability and local structure?

The pre-transition refractory high-entropy alloys (HEAs), such as NbMoTaW alloys, possess excellent thermal stability because of their single BCC structure and high melting point of the constituent element themselves, which is very well suited as candidates for the correlative research between the local structure and thermal stability. Furthermore, the alloys have enormous potential for applications in an extreme environment due to their excellent thermal stability, radiation resistance, oxidation resistance, high hardness, wear and corrosion resistance [1,2,8–12]. At present, many researches are performed in the alloy systems, for instance, NbMoTaW alloys melted by arc melting, exhibiting hardness of 4.46 GPa and compressive yield a strength of 1,058 MPa at RT; even at 1,200 °C, the latter value also can maintained at 506 MPa [13], which was attributed to the inhibition effect of solute diffusion and grain-boundary slipping due to the high configurational entropy. However, poor plasticity provides challenges for its fabrication and application. Their compressive plastic strains at RT range from 1.9 to 2.1% [14]. After adding V without changing the preparation method, the alloys still keep single BCC structures. The hardness and compressive yield strength are 5.42 and 2,612 GPa, respectively. The compressive yield strength still can reach 735 MPa at 1,200 °C. Unfortunately, the compressive plastic strain is reduced to 1.7% [13]. Utilizing mechanical alloying (MA) and spark plasma sintering (SPS) to prepare the NbMoTaW alloys, their ductility is significantly improved, showing 8.8% of the compressive plastic strain, and meanwhile, the compressive yield strength can be reached at 2,612 MPa, which is much higher than that of the alloy prepared by arc melting [15]. Obviously, the preparation method has an impact on the performance. The undesirable ductility is impossible to overcome if we only rely on micro-alloying without the change of the preparation method. However, conventional smelting or sintering is easier to produce the micro/macro-segregation, preparation defects, and change of the structural morphology. Arc smelting needs to face with the problems of higher cost and sample finite size. Mechanical alloying has a more complex preparation process and a long period. Compared with these bulk materials prepared by the above conventional methods, the preparation process of high-entropy thin films can avoid those difficulties, guaranteeing a more uniform composition distribution. Moreover, micro-segregation that is similar to the microstructure of bulky alloys can be avoided for the films, attributing to the near room-temperature preparation and fast forming velocity, which is beneficial to investigate the relationship between the local structure formed by relying solely on interatomic interactions and properties.

At present, there are few studies reported on high-entropy NbMoTaW films, which mainly focus on hardness and stability. The hardness of NbMoTaW films deposited on the Si(1 0 0) substrate utilizing direct current (DC) magnetron can reach 16 GPa, far higher than that of a bulk alloy [16,17]. Feng et al. [18] have analyzed the strengthening mechanisms contributed to the ultra-hardness of the films, which is relevant to grain size, including solution or grain-boundary strengthening and grain-boundary dislocation density. When the critical grain size is more than 40 nm, solid-solution strengthening plays a key role for the improvement of hardness. Otherwise, the main strengthening mechanism is grain-boundary strengthening. Except for ultra-hardness, thermal stability is another advantage for NbMoTaW films. In the previous studies, the 3-μm-thick NbMoTaW thin films with a grain size of about 70 ~ 150 nm were prepared by utilizing DC magnetron sputtering and ion beam-assisted deposition. After annealing at 1,100 °C for 3 days, the film maintains a uniform needle-like morphology, and its grain size does not grow up obviously, exhibiting good thermal stability, which is attributed to the insufficient driving force for grain-boundary migration due to its low grain boundary energy. More excitingly, the plasticity is significantly improved, compared with a bulk alloy and the compression plastic strain exceeds 30% [19]. Meanwhile, the films can still exhibit a BCC structure after 1-h oxidation in the air at 500 °C, exhibiting good oxidation resistance at high temperatures [20].

The objective of this paper is to explore the effects of local structure transformation brought about by the weak enthalpy-interaction-element, V, on the properties of an NbMoTaW system. To this end, a series of $(NbMoTaW)_{100-x}V_x$ ($x = 0 \sim 30.5$, at. %) thin films were prepared, using a radio frequency (RF) magnetron sputtering method. Through the systematic investigation of microstructures/compositions, the mechanical properties and the resistivity-temperature behavior of the films, the V-content dependence of properties of NbMoTaW films has been revealed. Furthermore, according to the "cluster-plus-glue-atom" model, the variation of the local structure with compositions was theoretically analyzed, indicating that the high stability of high-entropy films originates from the high melting point of the constituent element itself and microstructure fluctuations due to a high disorder degree and enthalpy interaction. This study provides a robust basis for the applications of refractory high entropy films in high-temperature bearing structures, heating protection systems, diffusion barriers, and film resistances.

2. Experimental section

2.1. Material preparation

With a JGP450 RF magnetron sputtering system, a series of refractory high-entropy $(NbMoTaW)_{100-x}V_x$ films were deposited on a single crystal Si (1 0 0) substrates. The Nb-Mo-Ta-W quaternary sputtering target [the purity of each component was not less than 99.9 weight percent (wt.%) with the diameter of 75 mm was prepared by powder hot pressing. In particular, the four elements of target have an equal atomic ratio. The Nb-Mo-Ta-W-V five-element alloy combination target were designed with vanadium pieces (Φ8 mm × 1 mm, the purity was not less than 99.9 wt.%) pasted in the main sputtering area of quaternary sputtering target. Films with different components were obtained by changing the number of V films (1 ~ 7) embedded in the sputtering process. The background vacuum is less than 3.0×10^{-4} Pa when the film is prepared under a 100 W RF power supply without bias, and the temperature of substrate was not higher than 323 K. The substrate rotated in a constant speed of 10 r/min, and the working distance was about 10 cm. Argon gas (99.999% purity) is filled to a pressure of about 2 Pa for build-up of luminance, and the argon gas flow is a 30 standard cubic centimeter per minute (sccm) during sputtering. The pre-sputtering time was 40 minutes, followed by 90 minutes of formal sputtering. In addition, the NbMoTaWV bulk alloy was fabricated by mechanical alloying with an equal ratio of five elements (purity 99.9 wt. %).

Table 1 shows the composition (Electron Probe Micro-analyzer spectrometric measurement) and thickness (Scanning Electron Microscopy cross-section analysis) measurements of as-deposited $(NbMoTaW)_{100-x}V_x$ ($x = 0 \sim 30.5$, at.%) films. The V content varies from 0 to 30.5 (at.%), while the other four metal components (Nb, Mo, Ta, and W) are close to the equal molar ratio. The film thickness does not change

Table 1
Film composition measured by EPMA and film thickness measured by SEM cross-section analysis.

Sample	Composition (at.%)					Thickness (nm)
	Nb	Mo	Ta	W	V	
NbMoTaW	23.66	22.95	25.15	28.24	0	463
$(NbMoTaW)_{96.0}V_{4.0}$	22.84	22.78	24.06	26.31	4.01	465
$(NbMoTaW)_{91.5}V_{8.5}$	21.95	22.39	23.07	24.13	8.46	460
$(NbMoTaW)_{87.1}V_{12.9}$	20.79	19.87	21.61	24.8	12.93	480
$(NbMoTaW)_{83.1}V_{16.9}$	19.78	19.29	20.42	23.64	16.87	480
$(NbMoTaW)_{78.7}V_{21.3}$	18.77	18.16	19.50	22.26	21.31	474
$(NbMoTaW)_{72.6}V_{27.4}$	17.45	17.08	17.59	20.53	27.35	460
$(NbMoTaW)_{69.5}V_{30.5}$	16.79	16.38	16.97	19.36	30.51	480

significantly with the increase of the V content, which is in the range of 460 ~ 480 nm.

2.2. Material characterizations

The composition of the film and bulk were analyzed with the wavelength dispersive spectrometer (WDS) of Electron Probe Micro-analyzer (EPMA, EPMA-1600, Shimadzu, Japan). Scanning electron microscopy (SEM, Zeiss Supra55, Baden-Wurttemberg, Germany) was used to measure the thicknesses. The crystal structures were investigated by Grazing-angle incidence X-ray diffraction (GIXRD, Bruker D8 Discover, Karlsruhe, Germany) and the chemical states were analyzed by X-ray photoelectron spectroscopy (XPS, EscaLab XI+, England). Transmission electron microscopy (TEM, Philips Tecnai G^2, Amsterdam, the Netherlands) and high-resolution transmission electron microscopy (HRTEM) were employed to characterize the microstructures and morphologies of the films. The composition distributions of the thin films were analyzed with the energy-dispersive x-ray spectroscopy (EDS) of the scanning transmission electron microscopy (STEM, FEI Talos F200X, the United States).

A nano-indenter (MTS XP, the United States) was performed for measuring the hardness and elasticity modulus of films, nine points were tested for each film and averaged. A four-point probe tester (RTS-9, 4 Probes Tech, Guangzhou, China) was applied for measuring the RT resistivity of films. The resistivity-temperature curve of films can be obtained by a thermal-resistance tester (TRT-1000, Wuhan, China), the testing temperature was set from RT to 1,078 K and heating rate was 10 K/min. After heating, the sample is cooled to room temperature by vacuum in the furnace. Surface current distribution was measured by atomic force microscopy (AFM, SPM-9700HT, Kyoto, Japan).

3. Results

3.1. Microstructural characterization

The microstructure of the as-deposited $(NbMoTaW)_{100-x}V_x$ ($x = 0 \sim 30.5$) films were investigated by GIXRD, with a grazing incident Angle of 1°, as presented in Fig. 1**(a)**. All films exhibit a single BCC structure. With the increase of the V content, all diffraction peaks gradually shifted to the right, indicating that the lattice parameters of the thin film decrease continuously, which can be ascribed to the substitutional solid solution of V with a smaller atomic radius. The lattice parameters of these films [Fig. 1 **(b)**] were obtained by full spectrum fitting, which varied from 0.3226 ± 0.0001 nm to 0.3179 ± 0.0001 nm.

The TEM analysis shows that the morphology of the as-deposited films is basically the same. Fig. 2 **(a)** shows the cross-sectional bright-field image of the $(NbMoTaW)_{72.6}V_{27.4}$ film, which indicates that the film is composed of nanocrystalline columnar crystals, and exhibits a smooth film-substrate interface with a uniform thickness. Furthermore, the film is identified as single-phase BCC structures by a selected area electron diffraction (SAED) pattern [Fig. 2 **(b)**], which is consistent with the GIXRD results. Fig. 2 **(c ~ d)** presents the bright and dark field images of $(NbMoTaW)_{91.5}V_{8.5}$ and $(NbMoTaW)_{69.5}V_{30.5}$ film,

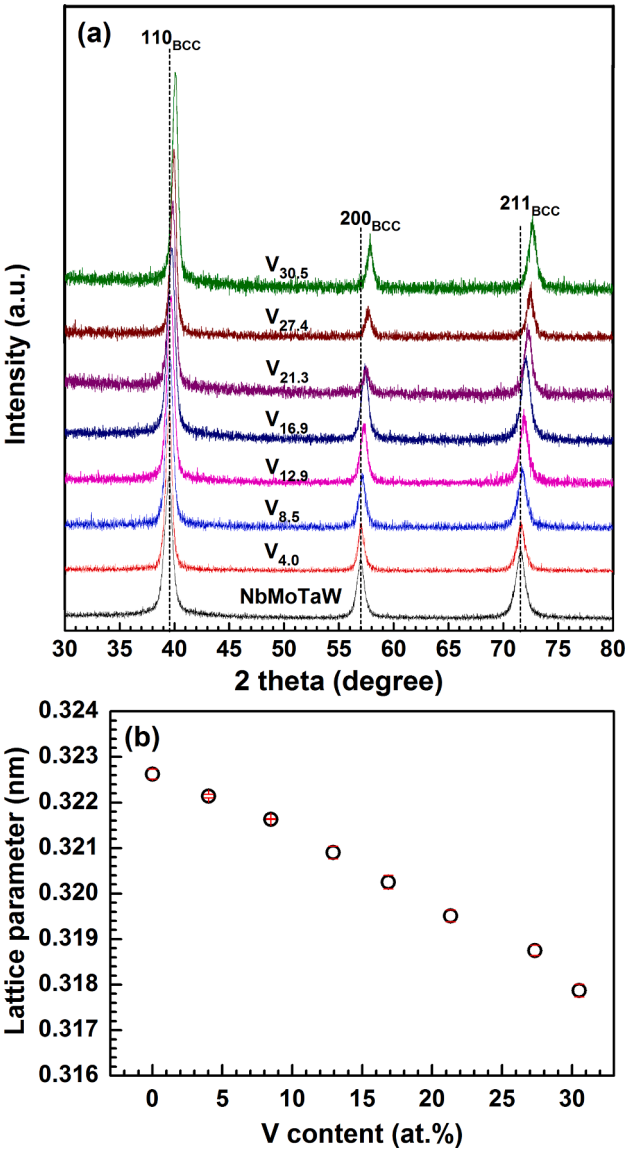

Fig. 1. GIXRD spectra of as-deposited $(NbMoTaW)_{100-x}V_x$ ($x = 0 \sim 30.5$) thin films (a), and lattice parameters of the thin films varying with the V content (b).

demonstrating a uniform grain-size distribution, and meanwhile its average grain size is 44 and 46 nm measured by a Nano Measurer 1.2 software [21], respectively. With the increase of the V content, the grain size of the films only changes slightly. Additionally, it is worth noting that the small contrast differences can be observed in a single grain interior, showing gray and white phases, which is necessary to be observed through larger magnification.

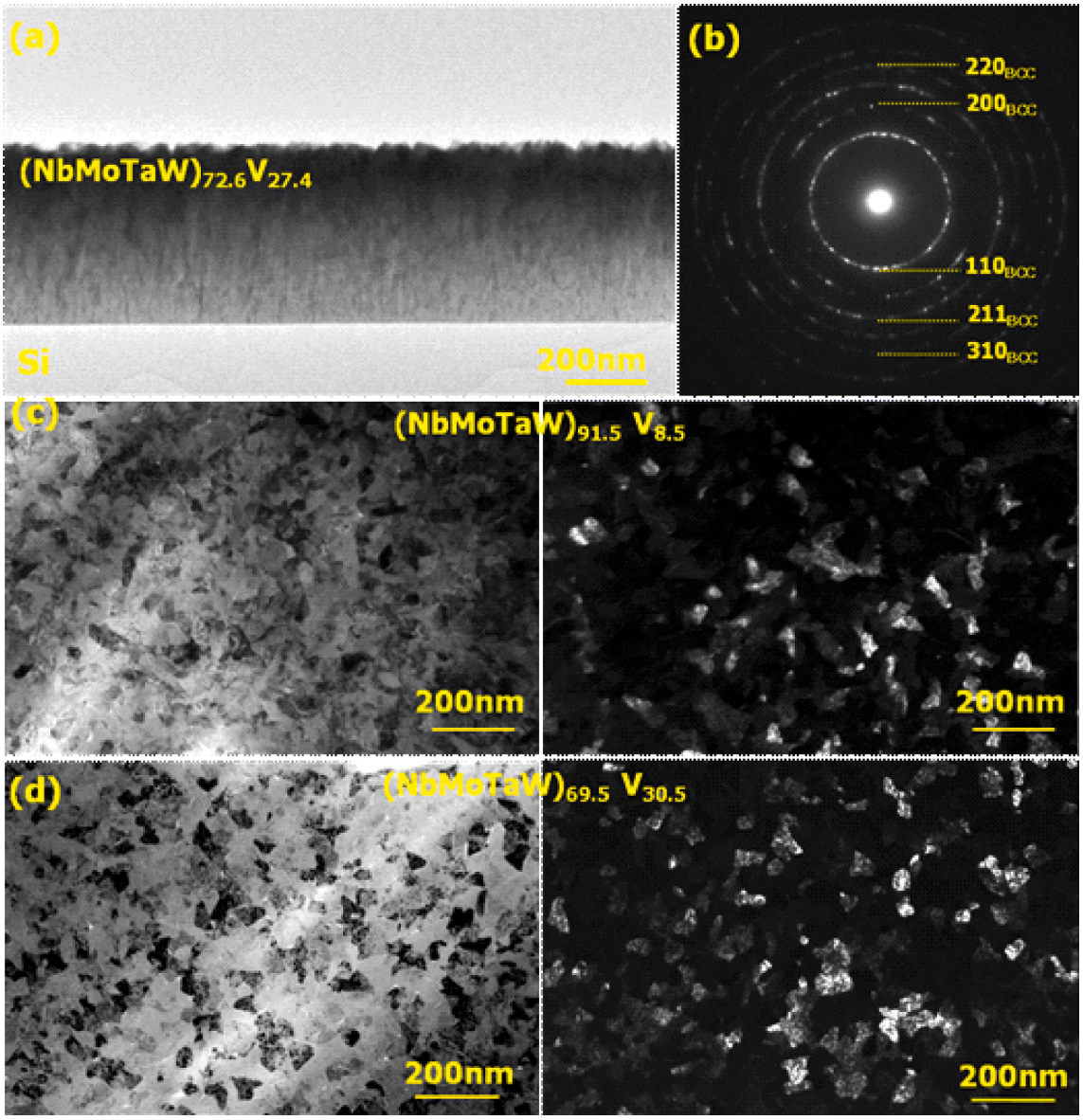

Fig. 2. Cross-sectional transmission electron microscopy (a) and selected transmission electron diffraction (b) of $(NbMoTaW)_{72.6}V_{27.4}$ film; Planar transmission electron microscopy (TEM) images of the bright field and dark fields of $(NbMoTaW)_{91.5}V_{8.5}$ and $(NbMoTaW)_{69.5}V_{30.5}$ films (c)~(d).

Fig. 3 **(a)** shows the planar high-resolution transmission electron microscopy (HRTEM) image of a single grain interior in the $(NbMoTaW)_{78.7}V_{12.9}$ film. The dual or single orientation filtering is performed for the HRTEM image, as presented in Fig. 3 **(b ~ d)**, which is obviously divided into two regions, distorted region (a yellow dotted frame), and non-distorted region (a red dotted frame). The small contrast difference on the dark-field image of a single grain is also caused by the difference of Bragg diffraction conditions of the distorted and non-distorted regions. There are complete and straight lattice fringes in the non-distorted region. However, many obvious lattice mismatch (dislocation) and distortion can be investigated in the distorted region, indicating a high-density lattice imperfection in the single grain, which would divide the grain into many small regions (sub-grains) with a size of about 2 – 4 nm.

The high-angle annular dark-field (HAADF) images of the as-deposited NbMoTaW, $(NbMoTaW)_{83.1}V_{16.9}$, or $(NbMoTaW)_{69.5}V_{30.5}$ films were observed by the STEM mode, as depicted in the Fig. 4 **(a ~ c)**, which exhibit a contrast differences between gray and white phases clearly. The contrast of the HAADF image is proportional to the square of the atomic number at the irradiation site of the electron beam. Thus, it can be determined that there exists a microscopic composition difference (segregation) in the films. For the V-free film, there are many white areas. However, the white areas are reduced after the V addition, especially for the $(NbMoTaW)_{69.5}V_{30.5}$ film, which indicates that the solid solution of V can reduce micro-segregation. According to the EDS mapping of the white area **[**Fig. 4 **(d)]** , Ta and W are relatively enriched in the film, which can be attributed to that they tend to be neighbored with each other due to their relatively-large negative mixing enthalpy (-7 kJ mol^{-1}). Therefore, the relatively-concentrated Ta and W with a large atomic number are bound to lead to the emergence of a bright image contrast on the HAADF images.

3.2. *Performance characterization of thin films*

3.2.1. *Mechanical properties of films*

The mechanical properties of $(NbMoTaW)_{100-x}V_x$ ($x = 0 \sim 30.5$) films were measured by nanoindentation with the fixed 300 nm of an indentation depth. The load-unloading curve are shown in Fig. 5 **(a)**. Normally, the elasticity of films can be represented by the elastic recovery coefficient, R [22].

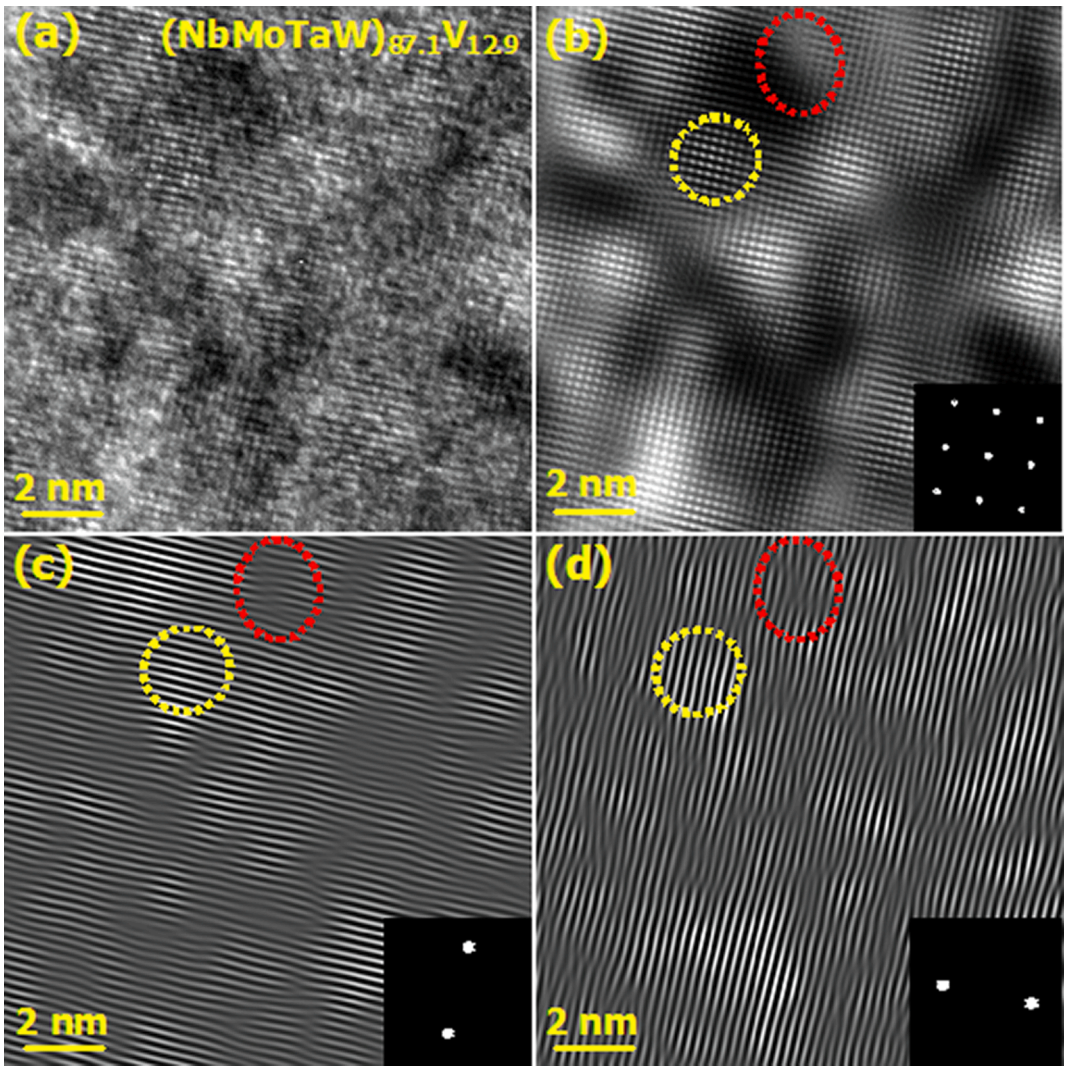

Fig. 3. HRTEM images (a) and filtered images of double-orientation (b) and single-orientation (c)~(d) of the $(NbMoTaW)_{87.1}V_{12.9}$ thin film.

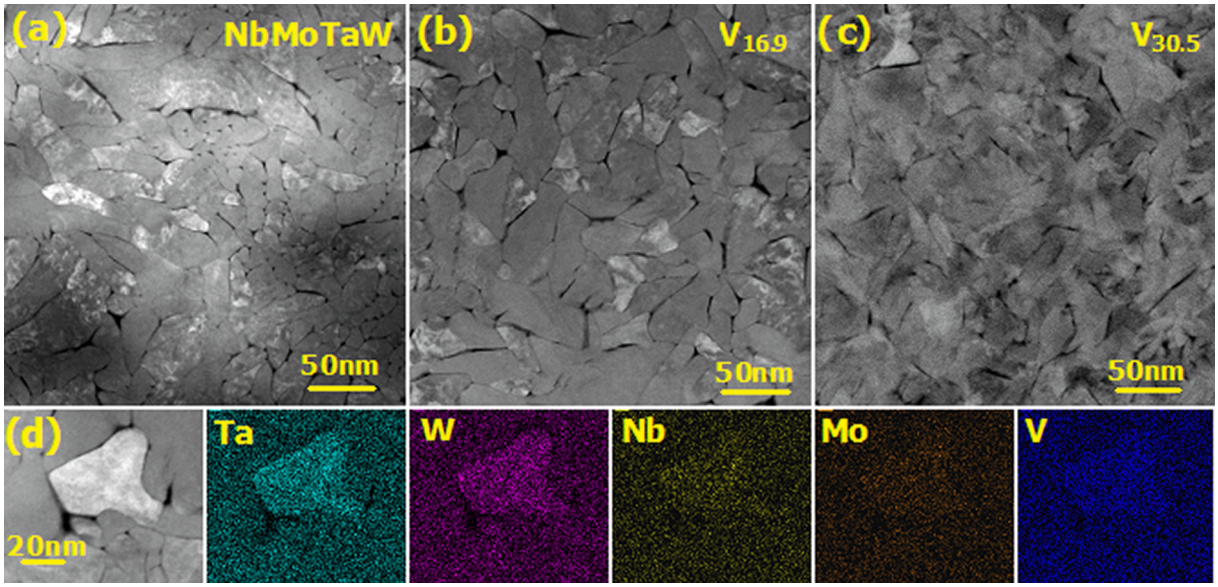

Fig. 4. STEM-HAADF images of NbMoTaW thin film (a), $(NbMoTaW)_{83.1}V_{16.9}$ thin film (b), and $(NbMoTaW)_{69.5}V_{30.5}$ thin film (c), and map analysis of the white region (d).

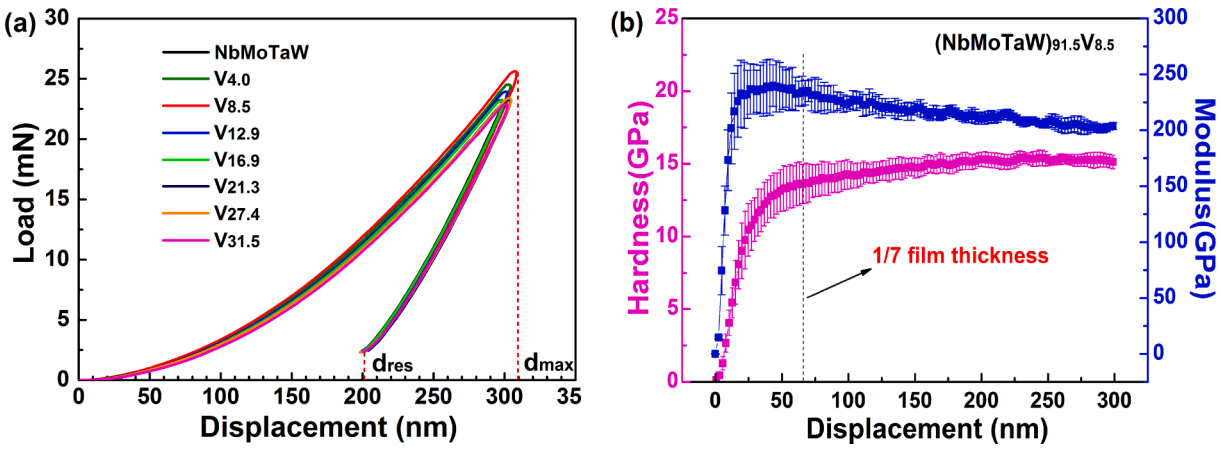

Fig. 5. Load-unloading curve of $(NbMoTaW)_{100-x}V_x (x = 0 \sim 30.5)$ film (a), hardness and modulus of $(NbMoTaW)_{91.5}V_{8.5}$ film with pressing depth of 300 nm (b).

$$R = \frac{(d_{max} - d_{res})}{d_{max}} \quad (1)$$

where d_{max} and d_{res} are the maximum displacement at loading and the minimum displacement at unloading, respectively. The elastic recovery-coefficient variation of $(NbMoTaW)_{100-x}V_x$ ($x = 0 \sim 30.5$) films, as shown in Fig. 6. With the increase of the V content, the elasticity of the film changes slightly, showing a tendency of increasing first and then decreasing. When the V content is 8.5%, the film elasticity is the highest, and the R is equal to 34.7%.

Elasticity modulus and hardness are the important property indication for the films, wherein the former is used to evaluate the elastic-deformation ability. Herein, the displacement dependence of hardness or elasticity modulus of the $(NbMoTaW)_{91.5}V_{8.5}$ film is presented in Fig. 5 **(b)**. In order to exclude the influence of the surface or matrix effect, the value of 1/7 of the film thickness is taken as the measured values in the hardness and modulus curves with the indentation depth. The displacement dependence of hardness or elasticity modulus of other films is shown in **Appendix**. Fig. 6 describes the hardness and elasticity modulus variation in the as-deposited $(NbMoTaW)_{100-x}V_x (x = 0 \sim 30.5)$ film. The hardness and elasticity modulus of NbMoTaW films are 12.16 ± 1.13 GPa and 227.89 ± 14.93 GPa, respectively. Adding a small amount of V, the hardness and elasticity modulus enhanced slightly as the V content increases, exhibiting a maximum value, 13.62 ± 1.36 GPa of hardness and 234.35 ± 13.85 GPa of elasticity modulus, when the V content reaches 8.5 at.%, respectively. However, continuing to increase the V content, the hardness and elasticity modulus of the film decrease slowly. When the V content reaches 30.5 at.%, their values are 9.70 ± 0.81 and 194.35 ± 12.25 GPa, respectively.

Friction and wear properties can be evaluated by utilizing the ratio between the hardness and elasticity modulus, H/E [23,24]. The H/E value of as-deposited $(NbMoTaW)_{100-x}V_x$ ($x = 0 \sim 30.5$) films are calculated according to the measured values (Fig. 6), showing 0.050 ~ 0.058, which is comparable to that of a metallic glass (H/E ≈ 0.050) [25]. With the increase of the V content, the H/E increases first and then decreases slightly, and the $(NbMoTaW)_{91.5}V_{8.5}$ film possesses a maximum value, equal to 0.058.

According to the above results, The V content has tiny influence on the mechanical properties of NbMoTaW films. However, their hardness, elasticity modulus, H/E, or elastic recovery coefficient, R, showing a similar variation tendency, increasing first and then decreasing slightly. Meanwhile, the variation in the V content is monotonically increasing, for V-free or V-containing films. They always keep a single BCC structure and a stable nanometer columnar crystal morphology. Therefore, the fluctuations of mechanical properties reflect atomic interactions evolutions at the microscopic scale. If only evaluating mechanical properties, the most outstanding properties can be obtained when the V content is equal to 8.5 at.%.

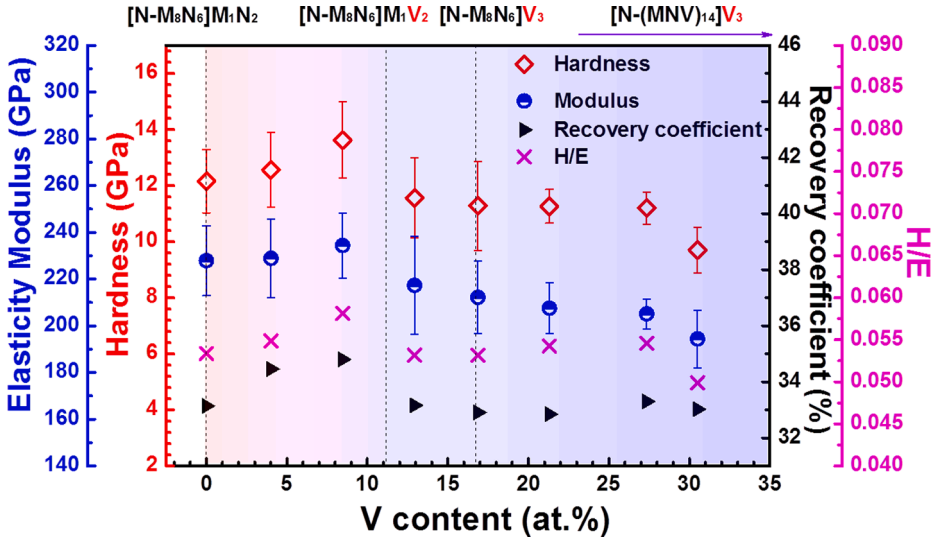

Fig. 6. The hardness, modulus, elastic-recovery coefficient and H/E of $(NbMoTaW)_{100-x}V_x$ ($x = 0 \sim 30.5$) films varying with the V content and clusters.

3.2.2. Temperature dependence of resistivity

The RT resistivity of $(NbMoTaW)_{100-x}V_x$ ($x = 0 \sim 30.5$) thin films were measured by the four-point probe technique, as shown in Fig. 7. The resistivity of the NbMoTaW thin film is 52.92 μΩ•cm. The resistivity improves, as the V content rises, and the value of the $(NbMoTaW)_{69.5}V_{30.5}$ film is 84.84 μΩ•cm, ascribing to the improvement of the disorder degree and the decrease of the number of valence electrons (increasing the content of the element with low electron number) due to the solid solution of V in the BCC structure. Compared with the above NbMoTaW film prepared by RF magnetron sputtering, the RT-resistivity values of NbMoTaW films prepared by DC magnetron sputtering are 168 ~ 170 μΩ•cm [14,16], which are significantly higher than the measured results in this paper. The reason is obviously related to difficulty in controlling DC magnetron sputtering processing and the drawback of the preparation method itself, resulting in the poor dense degree and heterogeneity of the films due to the high sputtering pressure or voltage, slow sputtering rate, easy to "discharge arc", and other phenomena. Fortunately, the RF magnetron sputtering can effectively prevent such problems because of its fast sputtering rate, high deposition rate, and relatively-uniform film layer [26,27]. Similar research results have been presented in the study of an AlCoCrFeNi high-entropy film [28].

Compared with the AlCoCrFeNi film (its resistivity is 428 μΩ•cm) prepared by RF magnetron sputtering, the resistivity of $(NbMoTaW)_{100-x}V_x$ ($x = 0 \sim 30.5$) thin films are lower, showing better electrical conductivity. According to the Weidmann - Franz's law, the ratio of the thermal conductivity to electrical conductivity of a metal is proportional to temperature in the normal temperature range [29]:

$$\frac{k}{\sigma T} = \frac{\pi^2}{3}\left(\frac{k_B}{e}\right)^2 = 2.44N10^{-8}W\Omega K^{-2} \equiv L_0 \quad (2)$$

where k is the thermal conductivity, σ is the electrical conductivity, T is the absolute temperature, k_B is the Boltzmann constant, e is the electron charge, and L_0 is called the Lorenz number. It can be inferred that the $(NbMoTaW)_{100-x}V_x$ film also has good thermal conductivity.

In order to understand the conductive mechanism of $(NbMoTaW)_{100-x}V_x$ films, the surface analysis of NbMoTaW, $(NbMoTaW)_{91.5}V_{8.5}$, $(NbMoTaW)_{72.6}V_{27.4}$, and $(NbMoTaW)_{69.5}V_{30.5}$ thin films was carried out by atomic force microscopy. Three-dimensional surface topographies and the surface-current distribution in the 1 μm × 1 μm region is shown in Fig. 8. In the surface-current distribution, blue and red regions represent the surface-conductivity difference. The blue region has good conductivity while the red region has bad conductivity. It can be seen that the current distribution of the NbMoTaW film has obvious fluctuation, and there are more blue areas. However, with the addition of the V content, the blue region and the current fluctuation decrease obviously. When the V content reaches 30.5%, the blue region is very few. In the $(NbMoTaW)_{100-x}V_x$ films, their microstructure always remains a BCC structure. Thus, the surface-current-distribution variation is closely related to the composition segregation. The addition of V is not only reducing the electrical-conductivity differences due to composition segregation, but also improving the homogeneity of composition or conductivity and increasing the resistivity, which are consistent with the STEM component analysis and resistivity measurements. In addition, the three-dimensional surface height and current diagram can be superimposed to eliminate the surface-current change caused by roughness, as shown in Fig. 8 **($c_1 \sim c_4$).**

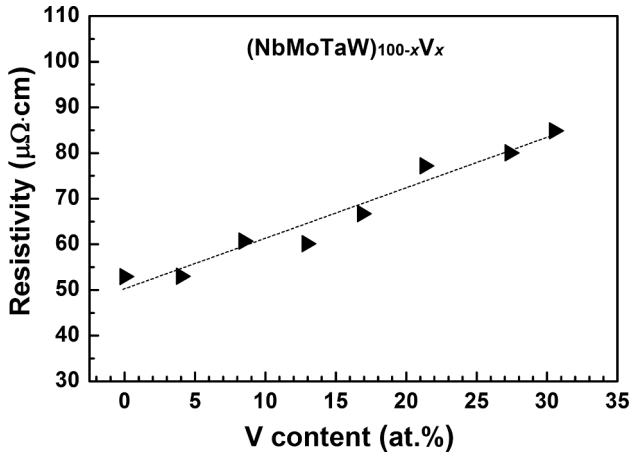

Fig. 7. Variation of the room-temperature resistivity of $(NbMoTaW)_{100-x}V_x$ ($x = 0 \sim 30.5$) films with the V content.

In order to further explore the thermal stability of the films, the resistivity of $(NbMoTaW)_{100-x}V_x$ ($x = 0 \sim 30.5$) films during the temperature increase from 373 to 1,073 K, developed by the variable temperature-resistance tester (two-point probe), as shown in Fig. 9. The RT resistivity of the films increases with the increase of the V content, which is coincided with the measured results through a four-point probe technology. During the heating process, the resistivity-temperature curves are divided into two stages according to the variation of each film. For the first stage, the curves exhibit a "plateaux" starting from RT, that is, the resistivity shows basically constant with the rising of temperature and the values can maintain stable from RT to nearly 873 K, indicating an excellent resistivity stability. With the increase of the V content, the "plateaux" would be narrow slightly, which reveals that the addition of V can induce the degradation of thermal stability. In the second stage, the resistivity decreases with increasing temperature, dropped below 50 μΩ•cm at 1,073 K.

Evidently, the described resistivity-temperature behavior above is caused by the high-entropy effect. For Nb, Mo, Ta, Wand V elements, their resistivities are 5–20 μΩ•cm at RT [30,31], which is far lower than that of the HEA thin films. Furthermore, their resistivity variation exhibits an upward trend with increasing the temperature (as exhibited in **Appendix**). In addition, the resistivity of AlCoCrFeNi HEA thin films maintains stable under 560 K while the resistivity of $(NbMoTaW)_{100-x}V_x$ ($x = 0 \sim 30.5$) thin films can stay stable from RT to nearly 873 K, exhibiting the more outstanding thermal stability, directly related to the fact that the constituent elements are all former transition metals with high melting points.

4. Discussion

4.1. Cluster analysis of thin-film composition

Microstructural investigation indicates that $(NbMoTaW)_{100-x}V_x$ high-entropy thin films always keep a single BCC structure, exhibiting a nanocrystalline columnar morphology. Hence, the local structure is the sole factor for driving a continuous change in the properties of disordered solid solutions with a single simple structure. Ideally, the "cluster-plus-glue-atom" model is the most appropriate model to describe such a specific local structure by atom occupancy [32]. In the model, metal elements with a negative mixing enthalpy tend to form characteristic local atomic clusters.

The "cluster-plus-glue-atom" structure model is constructed by Dong et al. [33,34], which describes the chemical short-range order through the first nearest-neighbor coordination polyhedron. In the model, the solute atoms are considered to form a first nearest-neighbor coordination polyhedron (cluster) in the matrix. Therefore, a stable solid solution can be illustrated through a specific local unit, which contains a cluster and a certain number of glue atoms, expressed as [cluster] $(\text{glue atoms})_x$.

According to the cluster definition, the cluster of a BCC lattice is CN14 type [35,36]. Its cluster formula can be expressed as [(center atom) -$(\text{shell atom})_{14}$]-$(\text{glue atom})_x$, (x being the integer number of glue atoms). In the formula, the cluster contains two sub-shells covering the eight nearest neighbors and the six next-nearest neighbors, forming a rhombic-dodecahedron **[**Fig. 10 **(a)]** , which is linked by 3 glue atoms.

According to the mixing enthalpy (ΔH), valance electron

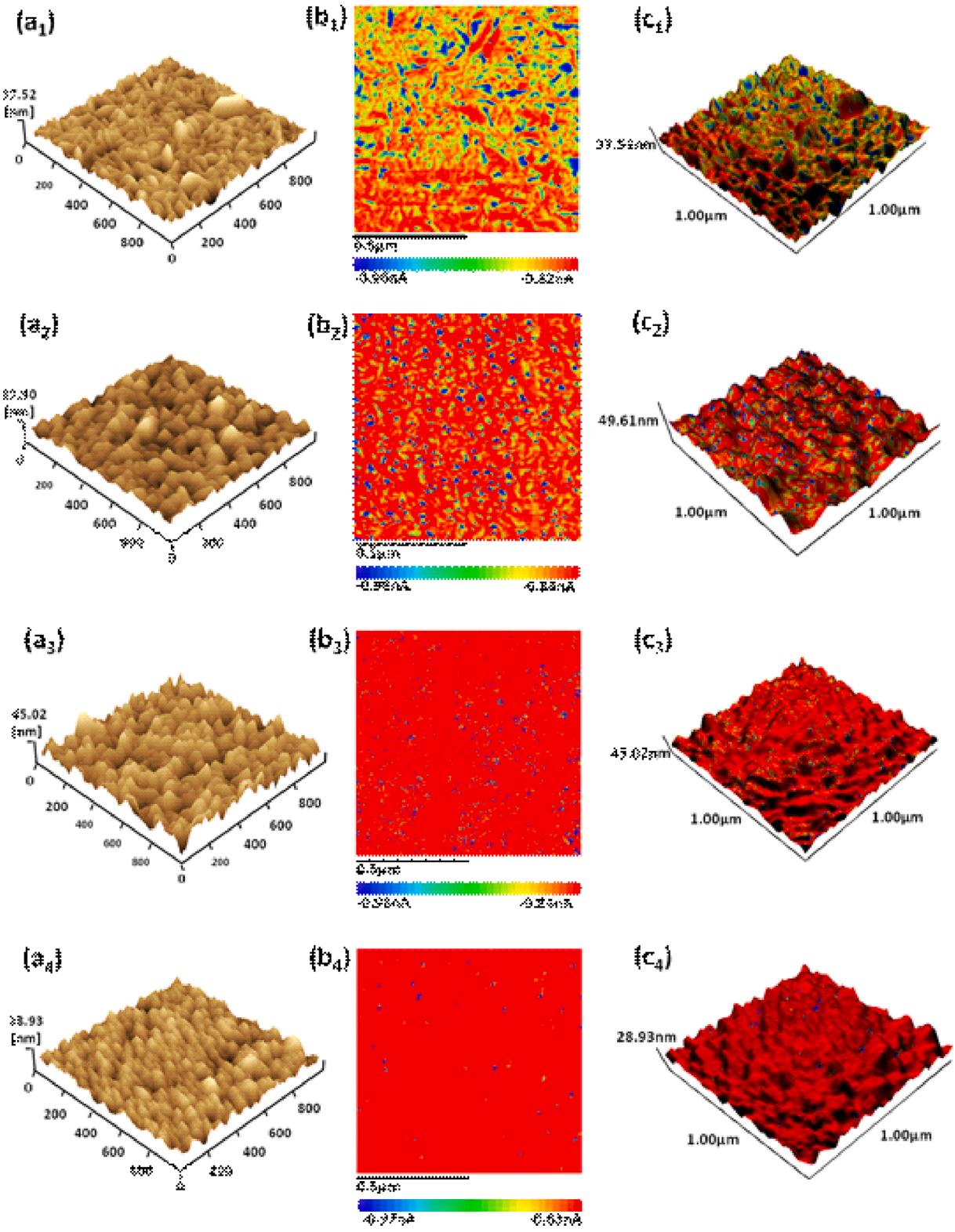

Fig. 8. Three-dimensional height diagrams ($a_1 \sim a_4$), the current distribution ($b_1 \sim b_4$), and three-dimensional image overlaying current distribution on the height diagrams ($c_1 \sim c_4$) of NbMoTaW, $(NbMoTaW)_{91.5}V_{8.5}$, $(NbMoTaW)_{72.6}V_{27.4}$, and $(NbMoTaW)_{69.5}V_{30.5}$ thin films.

concentration (VEC), and atomic radius of elements (as shown in Table 2), the component of the NbMoTaW high-entropy film can be divided into two kinds: the one is Nb and Ta, and the other one is Mo and W. For convenience of expression, the two types of elements can be represented by N-type and M-type, respectively. Among the same type of elements, they exhibit the same VEC, similar atomic radii, and 0 kJ mol^{-1} of mixing enthalpy between each other, which indicates that the same type of elements possesses the same atomic occupation position in the cluster formula construction. Therefore, considering the restriction of the equimolar ratio composition and mixing enthalpy, the NbMoTaW films with single BCC structures can be constructed as two types of cluster formulas if the N-type and M-type are center atoms, respectively,

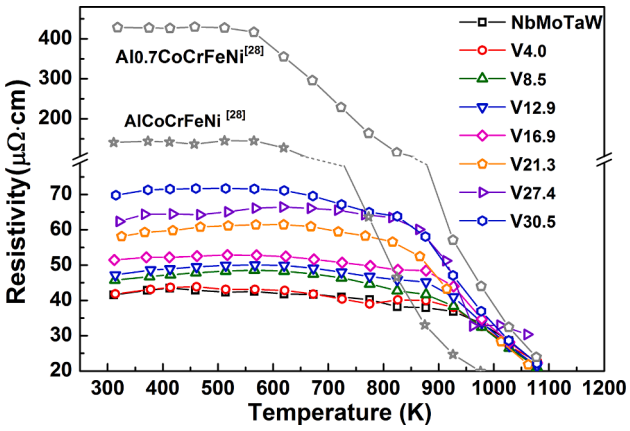

Fig. 9. Resistivity - temperature behavior of $(NbMoTaW)_{100-x}V_x(x = 0 \sim 30.5)$ films with reference to the AlCoCrFeNi films [28]

that is $[N\text{-}M_8N_6]M_1N_2$ [as shown in Fig. 10 **(b)**] and $[M{-}N_8M_6]N_1M_2$. It is not hard to found that the two cluster formulas are just observed from different angles, which are actually equivalent. Therefore, the first case as a typical condition for discussion in the paper.

For NbMoTaWV high-entropy films, the addition of V would preferentially occupy the glue atom position due to its small atomic radii and −1 or 0 kJ mol^{-1} of mixing enthalpy between V and other elements. Moreover, the VEC of V is the same as that of Nb or Ta, indicating that the three elements have similar nature. The V tends to replace the position of N-type atoms. Therefore, the cluster formula would gradually evolves into $[N\text{-}M_8N_6]M_1V_2$(the corresponding V content is equal to 11.11 at.%). Continue to increase the V content, the position of the M-type glue atom, would be substituted by V. When the V content reaches 16.67 at.%, the cluster formula exhibits $[N\text{-}M_8N_6]V_3$ by the V completely occupying the position of the glue atom, which is the maximum V content under the premise of an invariable cluster itself. If the V content further increases, the V atoms are inevitable to occupy the shell atom positions, and the cluster formula changes significantly, expressed by $[N\text{-}(MNV)_{14}]\text{-}V_3$.

4.2. Correlation relationship between mechanical properties and local structures

The hardness and elasticity modulus of the films tend to slight increase firstly and then decrease gradually, as the V content increases, which can be explained through cluster formula evolution under ideal conditions. For the V-free film, the cluster formula exhibits $[N\text{-}M_8N_6]M_1N_2$, and its atomic arrangement and interactions are presented in Fig. 11 **(a)**. Constrained by the mixing enthalpy, N-type elements as central atoms, and the first 8 M-type atoms and the last 6 N-type atoms are distributed in the shell. Moreover, according to the composition of an equal molar ratio, there must be 1 M-type atom and 2 N-type atoms in the position of glue atoms. For $[N\text{-}M_8N_6]M_1N_2$, there are strong interactions between the central atom and the first 8 M-type atoms, as well as the first 8 and the last 6 shell atoms, determining the stability of the cluster structure. Additionally, one strong interaction ($\Delta H1 = -7 \sim -8$ kJ mol^{-1}) and two weak interactions ($\Delta H2 = 0$ kJ mol^{-1}) are present between the clusters and glue atoms.

For the NbMoTaWV high-entropy thin films with a low V content (≤11.11 at.%), the V would preferentially substitute the N-type elements among the glue atoms due to the similar characters with N-type atoms. Meanwhile, the cluster formula changes to $[N\text{-}M_8N_6]M_1V_2$, as presented in Fig. 11 **(b)**, which have no influence on the original interaction between each other elements. However, the V is an added element with a small atomic radius, which would produce a displacement solution strengthening effect and relieve lattice distortion caused by the atomic-radius difference between M-type and N-type elements. Therefore, the hardness and modulus of films increase slightly. With increasing the V content continuously, the cluster formula would change to $[N\text{-}M_8N_6]V_3$ **[**Fig. 11 **(c)]**. The strong interactions between the M-type glue atoms and N-type shell atoms were replaced by the weak interaction between V and N-type atoms, resulting in loosening of the glue atoms parts in the cluster formula. Thus, the hardness and elasticity modulus gradually reduce. Next, a large number of V atoms are added (the V content **>** 16.67 at.%), it would occupy the position of shell atoms, and the local structure has to be adjusted to the $[N\text{-}(NM)_{14}]\text{-}V_3$ cluster formula **[**Fig. 11 **(d)]**. At this time, the cluster shell atoms are also loosened, the cluster formula structure is fundamentally altered, and the interaction between atoms is further weakened. Hence, the hardness and elasticity modulus are further reduced.

4.3. Resistivity-temperature behavior of thin films

The resistance of the transition metal high-entropy alloy film mainly originates from the following four crucial factors [28,37], including that (1) the scattering of electrons by a large amounts of grain boundaries caused by nanocrystalline columnar crystals, strengthening the

Table 2
Mixing enthalpy among five elements (Δ H), valance electron concentration (VEC), and atomic radii of Nb, V, Mo, Ta, and W.

Element	ΔH(kJ mol^{-1})					VEC	Atomic radius(Å)
	V	Nb	Ta	Mo	W		
V	—	−1	−1	0	−1	5	1.35
Nb	−1	—	0	−6	−8	5	1.47
Ta	−1	0	—	−5	−7	5	1.47
Mo	0	−6	−5	—	0	6	1.40
W	−1	−8	−7	0	—	6	1.41

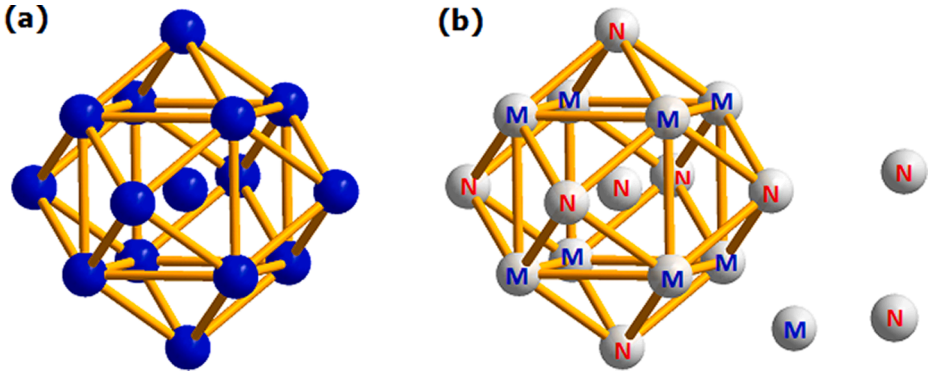

Fig. 10. The principal cluster schematic diagram of a BCC structure (a) and NbMoTaW high-entropy alloy (b) N and M represent the random distributions of Nb, Ta, Mo, and W, respectively.

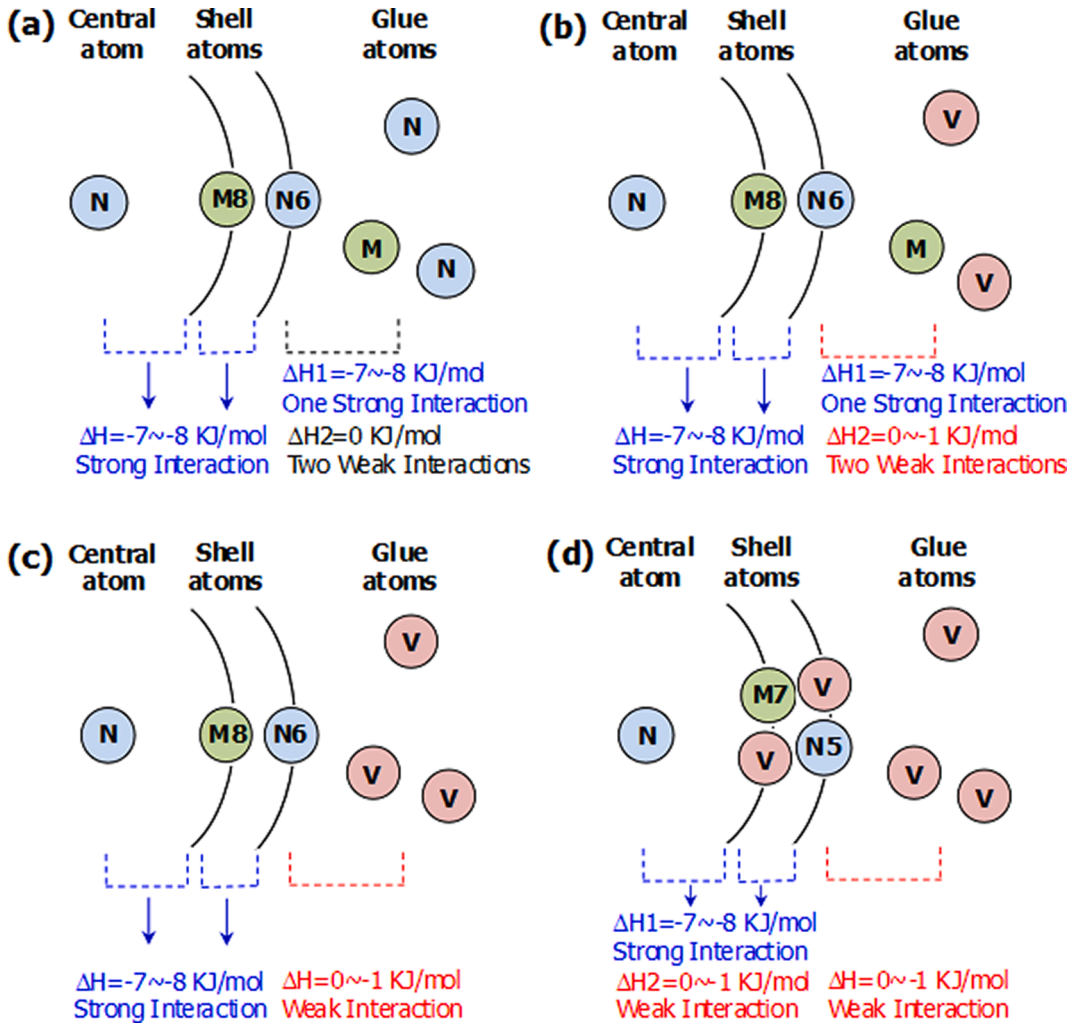

Fig. 11. Schematic diagram of atom interactions in $(NbMoTaW)_{100-x}V_x$ thin film clusters with the addition of V.

defection scattering; (2) the serious lattice distortion because of chemical disorder of multicomponent, enhancing the phonon scattering; (3) *s-d* scattering effect. It is a characteristic for transition metals that the d band is unfilled, and the conductive electrons include those from the unfilled d band and the filled s band. Under the action of an external field, scattered s electrons will transition to the d band, which reduces the mean free path of electrons and increases the resistance; and (4) the rising of the scattering effect due to the local spin interaction of magnetic elements. The existence of magnetic ions will induce exchange coupling with conduction electrons, resulting in the fact that the conduction electrons are scattered by local magnetic atoms repeatedly. This multiple scattering process enhances the barrier to electron motion so that the resistivity increases.

Compared with AlCoCrFeNi thin films, $(NbMoTaW)_{100-x}V_x$ ($x = 0 \sim 30.5$) high-entropy thin films exhibits lower resistivity, which includes three aspects of reasons. Firstly, the pre-transition elements (Nb, Mo, Ta, W, and V) have lower Fermi surface state densities [38], exhibiting relatively-small *s-d* scattering effect due to the difficult electron transition from *s* to *d* bands. Secondly, the magnetic elements (Co, Fe and Ni) contained in the AlCoCrFeNi films will increase the scattering effect on the conduction electrons. Finally, the addition of Al with a lower VEC (VEC = 3) [39] will reduce the number of valence electrons in the AlCoCrFeNi alloy and then increase the resistivity of the system.

The resistivity of $(NbMoTaW)_{100-x}V_x$ ($x = 0 \sim 30.5$) thin films (Fig. 9) can stay stable from RT to nearly 873 K, exhibiting excellent thermal stability. However, after the V addition, the thermal stability of V-containing films degrades slightly, which will be explained and discussed in the next section. When the temperature is higher than 873 K, the resistivity of V-free or V-containing films decreases dramatically, the reason of which is probably due to the phase transformation or disorder–order transition. The GIXRD was performed for the analysis of some films after the variable temperature-resistivity measurements, as presented in Fig. 12, which shows single BCC diffraction peaks in the XRD patterns of as-deposited films. After heating, single BCC diffraction peaks are separated into two different BCC phases (B1 and B2) diffraction peaks. The lattice parameters of the B1and B2 phases are 0.3414 nm and 0.3167 nm, respectively, according to the fitting result utilizing the Jade software [40]. From the standard peak position of Nb, Ta, Mo, W, and V shown in the Fig. 12, it can be found that the peak positions of B1 and B2 phases are close to those of N-type elements (Nb and Ta) with large lattice constants and that of M-type elements (Mo and W) with small lattice constants, respectively. Therefore, the diffraction peak split is the result of the aggregation of similar elements caused by the high-temperature disorder–order transition, and the resistivity drops sharply at the same time.

In order to uncover the source of the excellent resistivity stability of $(NbMoTaW)_{100-x}V_x$ ($x = 0 \sim 30.5$) thin films at high temperatures, the NbMoTaWV bulk alloy prepared by powder sintering was used for comparative analysis. Fig. 13**(a)** shows that the resistivity of the bulk alloy increases monotonously with the increase of temperature, without a plateau or sharp decline in the curve, which is the same as that of the pure metal. The metallurgical structures of the bulk alloy are presented

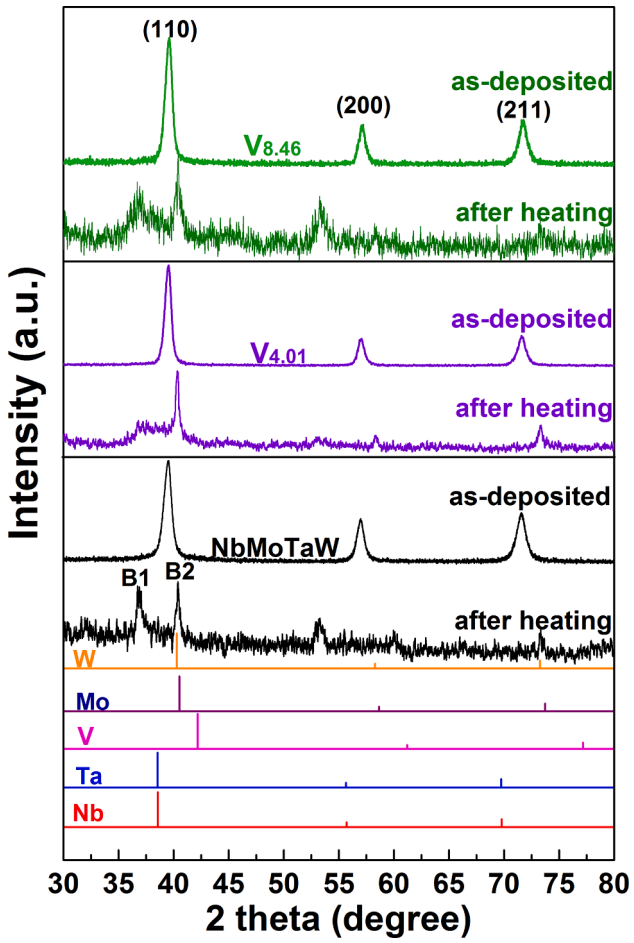

Fig. 12. GIXRD comparison of $(NbMoTaW)_{100-x}V_x$ thin films before and after temperature-resistance tests.

in Fig. 13**(b)**, exhibiting different corrosion-resistance regions due to a non-uniform distribution of microstructures or compositions. In addition, the wavelength dispersive spectrometer (WDS) analysis **[**Fig. 13 **(c)]** also indicates that the alloy is in a completely-segregated state, and the five components are not well mixed. Therefore, the favorable resistivity stability of $(NbMoTaW)_{100-x}V_x$ ($x = 0 \sim 30.5$) thin films at high temperatures first comes from its high disorder. However, with the addition of V, the disorder further increases while the high-temperature stability decreases slightly, indicating that the microscopic constituent fluctuations caused by the enthalpy interaction are also connected with the thermal stability of resistivity of thin films. Moreover, the thermal stability of the refractory component itself is also an important factor.

4.4. Influence of the V on the microstructure segregation and stability

In the NbMoTaW alloy system, there exists a relatively-large negative mixing enthalpy between the N-type elements (Nb and Ta) and M type elements (Mo and W), meanwhile between same kinds of atoms, showing a mixing enthalpy of 0 kJ mol^{-1}. According to the enthalpy interaction, different kinds of elements tend to be neighbors (strong interactions), and the same kind of elements has the opposite effect (weak interactions), which is easy to the production of micro-segregation. The results of STEM mapping also confirmed the existence of the Ta-W enrichment. Therefore, the enthalpy interaction can indeed drive the components to produce microscopic fluctuations under magnetron-sputtering conditions. When the V element, as a weak interaction component due to the minimal negative mixing enthalpy (0 ~ -1 kJ mol^{-1}) with other four elements, is added to decrease the interaction between atoms, resulting in the decrement of micro-segregation. In the analysis of the surface current, the composition fluctuation also can be observed in the NbMoTaW system, and tends to be more homogeneous with the addition of V. However, it is determining that the thermal stability of high-entropy films decreases, as the V content increases by the investigation of variable temperature resistivity, which indicates that there is no inevitable connection between the homogeneity and stability. In order to explore the stability, it is necessary to calculate the Gibbs free energy of $(NbMoTaW)_{100-x}V_x$ ($x = 0 \sim 30.5$) films.

According to Takeuchi and Inoue [41], the hypothesis of the multi-component alloy system was proposed. The Gibbs free energy (ΔG^{mix}) can be expressed as:

$$\Delta G^{mix} = \Delta H^{mix} - T\Delta S^{mix} \tag{3}$$

Here, T is the absolute temperature, ΔH^{mix} is the enthalpy of mixing, and ΔS^{mix} is the entropy of mixing.

In order to simplify the multicomponent alloy free-energy calculation, the regular solution model [42] can be used, and the enthalpy of the mixing ΔH^{mix} can use the following formula to calculate its value [43]:

$$\Delta H^{mix} = \sum_{i=1, i\neq j}^{n} \Omega_{ij} c_i c_j \tag{4}$$

where Ω_{ij} ($=4H^{mix}_{AB}$) is the regular solution interaction parameter of the ith and jth elements. c_i and c_j are the percentages of atomic elements for the ith and jth elements, respectively. H^{mix}_{AB} is for the binary alloy liquid mixing enthalpy [44].

According to the Boltzmann hypothesis, the mixing entropy of a multi-component alloy is [43]:

$$\Delta S^{mix} = -R\sum_{i=1}^{n}(c_i \ln c_i) \tag{5}$$

where c_i is the molar percentage of components and R ($=8.314$ J K^{-1} mol^{-1}) is the gas constant. It can be seen that the mixing entropy is the highest for the equiatomic ratio alloy.

According to the formulas (3) - (5), the ΔS^{mix}, ΔH^{mix}, and ΔG^{mix} values of $(NbMoTaW)_{100-x}V_x$ ($x = 0 \sim 30.5$) thin films can be calculated, as listed in Table 3. The ΔS^{mix} of the V-containing alloy is significantly higher than that of the V-free alloy, and meanwhile a higher ΔS^{mix} exists in the multicomponent alloys with equal/nearly-equal atomic ratios, compared with other traditional alloys. With increasing the content of the small radius atoms, V, the ΔH^{mix} and ΔG^{mix} values increase. Therefore, combining with theoretical calculation and practical measurement results, it shows that the addition of V brings two effects. On one hand, the disorder of the film increases, and it becomes more uniform. On the other hand, the system energy gradually increases, and the stability of the film decreases due to the decrement of the average interatomic interaction in the film.

Further chemical shift measurements with XPS can obtain experimental evidence that the addition of V changes the interaction between atoms. The NbMoTaW, $(NbMoTaW)_{91.5}V_{8.5}$, and $(NbMoTaW)_{78.7}V_{21.3}$ films are selected for comparative analysis, as shown in Fig. 14 **(a)**. Because the sample surface is in a state of native oxidation, each element has two metal peaks at the low energy end and two oxidation peaks at the high-energy end. First of all, the native oxidation peaks of the high entropy films are lower than the metal elements. Taking Ta as an example, the native oxide is Ta_2O_5 for a pure metal element while the native oxide peak of Ta is between TaO_2 and Ta_2O_5 in NbMoTaW, $(NbMoTaW)_{91.5}V_{8.5}$, and $(NbMoTaW)_{78.7}V_{21.3}$ high-entropy films, indicating that the high-entropy film exhibits outstanding oxidation resistance. Moreover, the V addition induces a considerable increase in the relative intensity of the oxidation peak as well as the shifting of the metal peak to the high energy, indicating the aggravated oxidation

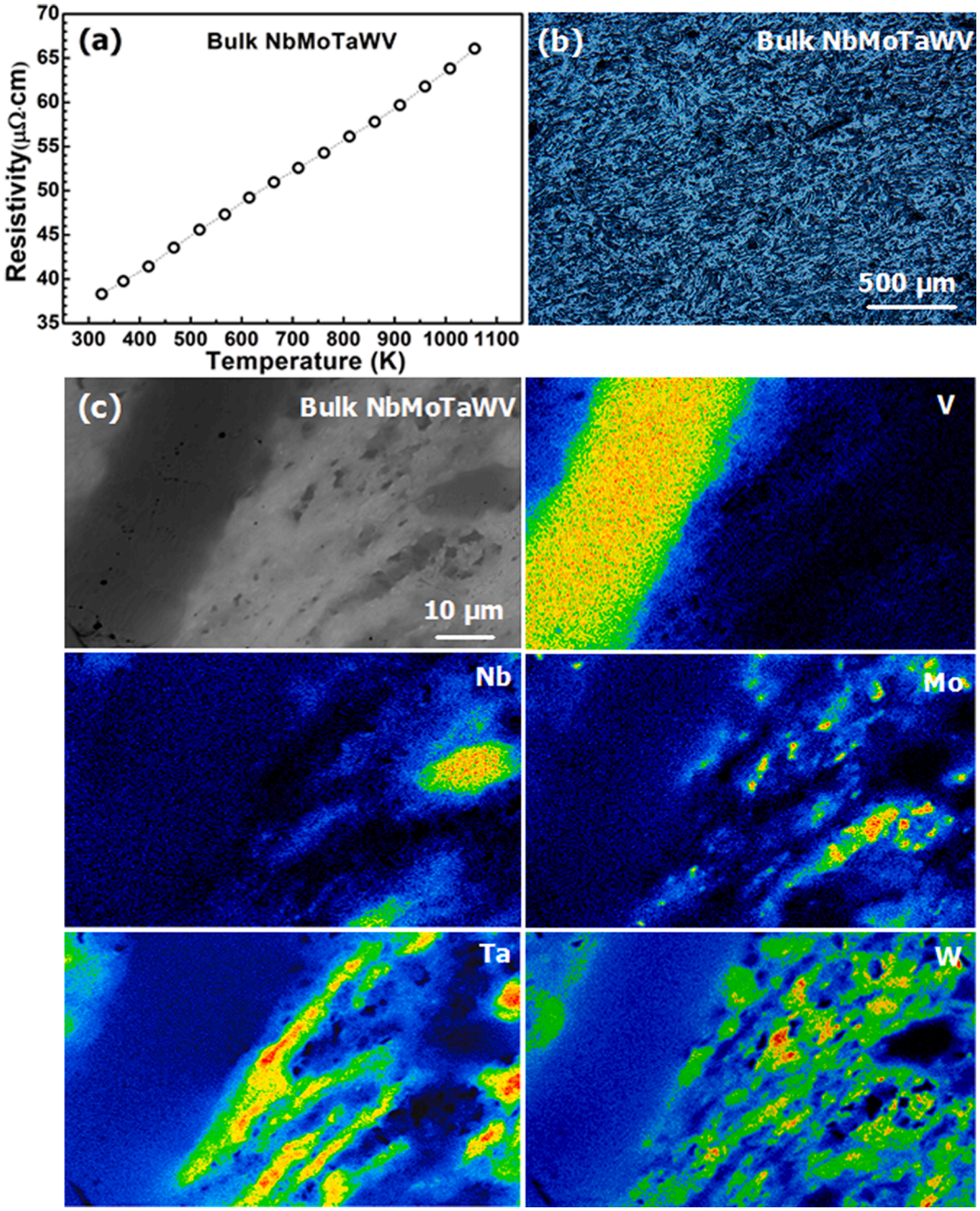

Fig. 13. Resistivity-temperature curve (a), metallographic morphology (b), and energy spectrum map scanning (c) analysis of the bulk NbMoTaWV alloy.

Table 3
The ΔS^{mix}, ΔH^{mix} and ΔG^{mix} of $(NbMoTaW)_{100-x}V_x$ ($x = 0 \sim 30.5$) films.

Sample	Composition (at.%)	ΔS^{mix}(J K^{-1} mol^{-1})	ΔH^{mix}(kJ mol^{-1})	ΔG^{mix}(kJ mol^{-1})
1	(NbMoTaW)	11.50	−6.58	−10.01
2	$(NbMoTaW)_{96.0}V_{4.0}$	12.45	−6.16	−9.87
3	$(NbMoTaW)_{91.5}V_{8.5}$	12.96	−5.70	−9.56
4	$(NbMoTaW)_{87.1}V_{12.9}$	13.21	−5.35	−9.28
5	$(NbMoTaW)_{83.1}V_{16.9}$	13.33	−4.98	−8.95
6	$(NbMoTaW)_{78.7}V_{21.3}$	13.36	−4.59	−8.58
7	$(NbMoTaW)_{72.6}V_{27.4}$	13.23	−4.08	−8.02
8	$(NbMoTaW)_{69.5}V_{30.5}$	13.11	−3.82	−7.73

(surface oxidation will increase the electron binding energy in the inner layer of metal elements, the more electrons are lost in oxidation, the greater the increase), which is another powerful evidence for the reduction in thermal stability.

Next, to avoid the disturbance of surface oxidation on the chemical shift, the XPS analysis was performed after etching the top of films of 100 nm. The measured results are shown in Fig. 14**(b)**, exhibiting that the sole metal peaks exist in these spectra. It can be indicated that the chemical shifts of N-type atoms (Nb and Ta) remain basically unchanged after the addition of V, while the peak positions of M-type atoms (Mo and W) are slightly shifted to the low-energy ends, confirming that the atomic interactions are indeed weakened.

Obviously, the weakening of interatomic interaction caused by V leads to the decrease of thermal stability of the film, and this effect is more and more obvious with the increase of the content of V.

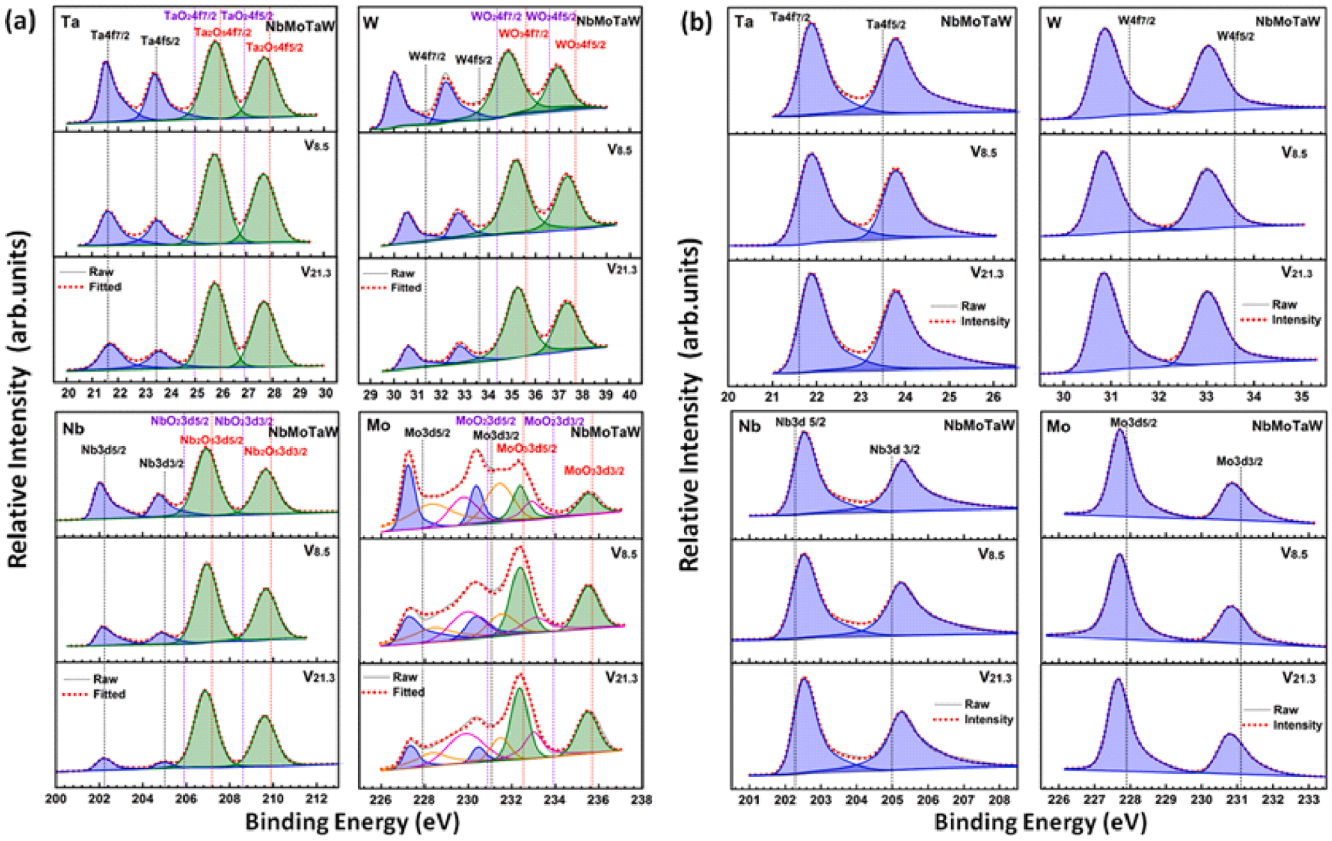

Fig. 14. XPS analysis of NbMoTaW, $(NbMoTaW)_{91.5}V_{8.5}$, and $(NbMoTaW)_{78.7}V_{21.3}$ thin films before (a) and after being etched at 100 nm (b).

5. Conclusion

To explore the influence of the local-structure evolution caused by the weak interaction element on the properties of refractory high-entropy thin films, a series of $(NbMoTaW)_{100-x}V_x$ ($x = 0 \sim 30.5$, at.%) thin films were prepared by RF magnetron sputtering. According to the investigation on the microstructure/composition, mechanical properties, resistivity temperature behavior of thin films, and the compositional interpretation based on the "clusters plus glue atom" model, the following conclusions can be drawn. The high-entropy NbMoTaW alloy thin films show a single-phase BCC structure, while presenting micro-segregation of Ta and W caused by microscopic composition fluctuations due to the enthalpy-interaction behavior. The addition of V brings a tine fluctuate in the mechanical properties of NbMoTaW thin films. The elastic-recovery coefficient, hardness, elasticity modulus, and hard-elastic ratio of the films show a trend of the slight increase first and then slowly decline as the V content increases, attributing to the variation of interactions between microscopic scale atoms. In particular, the $(NbMoTaW)_{91.5}V_{8.5}$ film possesses the best mechanical properties, exhibiting the hardness of 13.62 ± 1.36 GPa, elasticity modulus of 234.35 ± 13.85 GPa, and hard elastic ratio of 0.058, respectively. Compared with AlCoCrFeNi films, $(NbMoTaW)_{100-x}V_x$ films show lower resistivity. With the increase of the V content solid solution in the BCC structure, the resistivity of films increases from 52.92 to 84.84 μΩ•cm at room temperature. Meanwhile films show the excellent resistivity thermal stability, which is closely related to the high disorder degree, the microstructural fluctuation due to the enthalpy interaction as well as the high stability of the refractory component itself. According to the theoretical calculation and practical research results, the addition of V not only improves the disorder of the film to obtain a more uniform film, but also makes the average atomic interaction of the film gradually weaken, leading to the energy of the system increases, and the stability of the film decreases. The refractory high-entropy film has high hardness and excellent high-temperature resistance, which is conducive to its applications in the high-temperature-bearing structure, heat-protection system, diffusion barrier and film resistors, and other fields of high-temperature resistance, high hardness and wear resistance.

CRediT authorship contribution statement

Linxia Bi: Writing - original draft, Data curation, Formal analysis, Investigation. **Xiaona Li:** Conceptualization, Methodology, Supervision, Formal analysis. **Yinglin Hu:** Formal analysis, Writing - review & editing. **Junyi Zhang:** Writing - review & editing. **Xiao Wang:** Writing - review & editing. **Xuecheng Cai:** Resources. **Tongde Shen:** Resources. **Renwei Liu:** Resources. **Qing Wang:** Conceptualization. **Chuang Dong:** Conceptualization. **Peter K. Liaw:** Writing - review & editing, Supervision.

Declaration of Competing Interest

The authors declare that they have no known competing financial interests or personal relationships that could have appeared to influence the work reported in this paper.

Acknowledgements

We gratefully acknowledge the financial supports by the National Natural Science Foundation of China (Grant No. 52071052), the Science Challenge Project (TZ2016004), the National Defense Basic Scientific Research Project (2020-JCJQ-ZD-157) & the National Science Foundation (DMR-1611180 and 1809640) with the program directors, Drs. J. Yang, G. Shiflet, and D. Farkas.

Appendix A. Supplementary data

Supplementary data to this article can be found online at https://doi.org/10.1016/j.apsusc.2021.150462.

References

[1] D.B. Miracle, O.N. Senkov, A critical review of high entropy alloys and related concepts, Acta. Mater. 122 (2017) 448–511.
[2] W.R. Zhang, P.K. Liaw, Y. Zhang, Science and technology in high-entropy alloys, Sci. China. Mater. 61 (2018) 2–22.
[3] Q.J. Li, H. Sheng, E. Ma, Strengthening in multi-principal element alloys with local-chemical-order roughened dislocation pathways, Nat. Commun. 10 (2019) 3563.
[4] Q.Q. Ding, Y. Zhang, X. Chen, X.Q. Fu, D.K. Chen, S.J. Chen, L. Gu, F. Wei, H.B. Bei, Y.F. Gao, M.R. Wen, J.X. Li, Z. Zhang, T. Zhu, R.O. Ritchie, Q. Yu, Tuning element distribution, structure and properties by composition in high-entropy alloys, Nature 574 (2019) 223–227.
[5] Y. Dong, K.Y. Zhou, Y.P. Lu, X.X. Gao, T.M. Wang, T.J. Li, Effect of vanadium addition on the microstructure and properties of AlCoCrFeNi high entropy alloy, Mater. Des. 57 (2014) 67–72.
[6] J.B. Cheng, X.B. Liang, B.S. Xu, Effect of Nb addition on the structure and mechanical behaviors of CoCrCuFeNi high-entropy alloy coatings, Surface & Coatings Technology, Surf. Coat. Tech. 240 (2014) 184–190.
[7] J. Zhang, Y.Y. Hu, Q.Q. Wei, Y. Xiao, P.A. Chen, G.Q. Luo, Q. Shen, Microstructure and mechanical properties of Re_xNbMoTaW high-entropy alloys prepared by arc melting using metal powders, J. Alloy. Compd. 827 (2020), 154301.
[8] B. Cantor, I.T.H. Chang, P. Knight, A.J.B. Vincent, Microstructural development in equiatomic multicomponent alloys, Mate. Sci. Eng. A. 375–377 (2004) 213–218.
[9] Y.F. Ye, Q. Wang, J. Lu, C.T. Liu, Y. Yang, High-entropy alloy: challenges and prospects, Mater. Today 19 (2016) 349–362.
[10] O.N. Senkov, G.B. Wilks, D.B. Miracle, C.P. Chuang, P.K. Liaw, Refractory high-entropy alloys, Intermetallics 18 (2010) 1758–1765.
[11] O.N. Senkov, D.B. Miracle, K.J. Chaput, Development and exploration of refractory high entropy alloys—A review, J. Mater. Res. 33 (2018) 3092–3128.
[12] Y. Zhang, T.T. Zuo, Z. Tang, M.C. Gao, K.A. Dahmen, P.K. Liaw, Z.P. Lu, Microstructures and properties of high-entropy alloys, Prog. Mater. Sci. 61 (2014) 1–93.
[13] O.N. Senkov, G.B. Wilks, J.M. Scott, D.B. Miracle, Mechanical properties of $Nb_{25}Mo_{25}Ta_{25}W_{25}$ and $V_{20}Nb_{20}Mo_{20}Ta_{20}W_{20}$ refractory high entropy alloys, Intermetallics 19 (2011) 698–706.
[14] Z.D. Han, H.W. Luan, X. Liu, N. Chen, X.Y. Li, Y. Shao, K.F. Yao, Microstructures and mechanical properties of Ti_xNbMoTaW refractory high-entropy alloys, Mate. Sci. Eng. A. 712 (2018) 380–385.
[15] B. Kang, J. Lee, H.J. Ryu, S.H. Hong, Ultra-high strength WNbMoTaV high-entropy alloys with fine grain structure fabricated by powder metallurgical process, Mate. Sci. Eng. A. 712 (2018) 616–624.
[16] X.B. Feng, J.Y. Zhang, Z.R. Xia, W. Fu, K. Wu, G. Liu, J. Sun, Stable nanocrystalline NbMoTaW high entropy alloy thin films with excellent mechanical and electrical properties, Mater. Lett. 210 (2018) 84–87.
[17] H. Kim, S. Nam, A. Roh, M. Son, M.H. Ham, J.H. Kim, H. Choi, Mechanical and electrical properties of NbMoTaW refractory high-entropy alloy thin films, Int. J. Refract. Met. H. 80 (2019) 286–291.
[18] X.B. Feng, J.Y. Zhang, Y.Q. Wang, Z.Q. Hou, K. Wu, G. Liu, J. Sun, Size effects on the mechanical properties of nanocrystalline NbMoTaW refractory high entropy alloy thin films, Int. J. Plasticity 95 (2017) 264–277.
[19] Y. Zou, H. Ma, R. Spolenak, Ultrastrong ductile and stable high-entropy alloys at small scales, Nat. Commun. 6 (2015) 7748.
[20] Y.Y. Chen, S.B. Hung, C.J. Wang, W.C. Wei, J.W. Lee, High temperature electrical properties and oxidation resistance of V-Nb-Mo-Ta-W high entropy alloy thin films, Surf. Coat. Tech. 375 (2019) 854–863.
[21] Q. Xiao, Y. Sun, J. Zhang, Q.J. Li, Size-dependent of chromium (VI) adsorption on nano α-Fe_2O_3 surface, Appl. Surf. Sci. 356 (2015) 18–23.
[22] J.Y. Zhang, B. Zhang, Q.J. Xue, Z. Wang, Ultra-elastic recovery and low friction of amorphous carbon films produced by a dispersion of multilayer graphene, Diam. Relat. Mater. 23 (2012) 5–9.
[23] A. Leyland, A. Matthews, On the significance of the H/E ratio in wear control: a nanocomposite coating approach to optimised tribological behaviour, Wear 246 (2000) 1–11.
[24] R.C.D. Richardson, The wear of metals by relatively soft abrasives, Wear 11 (1968) 245–275.
[25] W.H. Wang, The elastic properties, elastic models and elastic perspectives of metallic glasses, Prog. Mater. Sci. 57 (2012) 487–656.
[26] F. Kurdesau, G. Khripunov, A.F. da Cunha, M. Kaelin, A.N. Tiwari, Comparative study of ITO layers deposited by DC and RF magnetron sputtering at room temperature, J. Non. Cryst. Solids 352 (2006) 1466–1470.
[27] J.O. Parka, J.H. Leea, J.J. Kima, S.H. Choa, Y.K. Cho, Crystallization of indium tin oxide thin films prepared by RF-magnetron sputtering without external heating, Thin. Solid. Films 474 (2005) 127–132.
[28] C.Y. Wang, X.N. Li, Z.M. Li, Q. Wang, Y.H. Zheng, Y. Ma, L.X. Bi, Y.Y. Zhang, X. H. Yuan, X. Zhang, C. Dong, P.K. Liaw, The resistivity - temperature behavior of Al_xCoCrFeNi high-entropy alloy films, Thin. Solid. Films 700 (2020), 137895.
[29] K. Tankeshwar, N.H. March, Relation Between Electrical and Thermal Conductivities in Charged Condensed Phases, Phys. Ckrm. Liq. 31 (1996) 39–47.
[30] R.E. Taylor, R.A. Finch, The specific heats and resistivities of molybdenum, tantalum, and rhenium, J. Less. Common. Metals 6 (1964) 283–294.
[31] G. Dyos, T. Farrell, The Handbook of Electrical Resistivity : New materials and pressure effects, The Institution of Engineering and Technology, London, United Kingdom, 2012.
[32] J.X. Chen, Q. Wang, Y.M. Wang, J.B. Qiang, C. Dong, Cluster formulae for alloy phases, Phil. Mag. Lett. 90 (2010) 683–688.
[33] Y. Ma, Q. Wang, C.L. Li, L.J. Santodonato, M. Feygenson, C. Dong, P.K. Liaw, Chemical short-range orders and the induced structural transition in high-entropy alloys, Scr. Mater. 144 (2018) 64–68.
[34] C. Dong, Q. Wang, J.B. Qiang, Y.M. Wang, N. Jiang, G. Han, Y.H. Li, J. Wu, J. H. Xia, From clusters to phase diagrams: composition rules of quasicrystals and bulk metallic glasses, J. Phys. D: Appl. Phys. 40 (2007) R273–R291.
[35] C. Pang, Q. Wang, R.Q. Zhang, Q. Li, X. Dai, C. Dong, P.K. Liaw, β Zr–Nb–Ti–Mo–Sn alloys with low Young's modulus and low magnetic susceptibility optimized via a cluster-plus-glue-atom model, Mater. Sci. Eng. A. 626 (2015) 369–374.
[36] C. Pang, B.B. Jiang, Y. Shi, Q. Wang, C. Dong, Cluster-plus-glue-atom model and universal composition formulas [cluster](glue atom)$_x$ for BCC solid solution alloys, J. Alloys. Compd. 652 (2015) 63–69.
[37] L. Kouwenhoven, L. Glazman, Revival of the Kondo effect, Phys. World 14 (2001) 33–38.
[38] N.F. Mott, Electrons in transition metals, Adv. Phys. 13 (2006) 325–422.
[39] S. Guo, C. Ng, J. Lu, C.T. Liu, Effect of valence electron concentration on stability of fcc or bcc phase in high entropy alloys, J. Appl. Phys. 109 (2011), 103505.
[40] T.P. Chou, Q.F. Zhang, G.E. Fryxell, G.Z. Cao, Hierarchically Structured ZnO Film for Dye-Sensitized Solar Cells with Enhanced Energy Conversion Efficiency, Adv. Mater. 19 (2007) 2588–2592.
[41] A. Takeuchi, A. Inoue, Quantitative evaluation of critical cooling rate for metallic glasses, Mater. Sci. Eng. A. 304–306 (2001) 446–451.
[42] B. Sundman, J. Agren, A regular solution model for phases with several components and sublattices, suitable for computer applications, J. Phys. Chem. Solids 42 (1981) 297–301.
[43] X. Yang, Y. Zhang, Prediction of high-entropy stabilized solid-solution in multi-component alloys, Mater. Chem. Phys. 132 (2012) 233–238.
[44] A. Takeuchi, A. Inoue, Classification of Bulk Metallic Glasses by Atomic Size Difference, Heat of Mixing and Period of Constituent Elements and Its Application to Characterization of the Main Alloying Element, Mater. Trans. 46 (2005) 2817–2829.